# Nanoscale

Accepted Manuscript


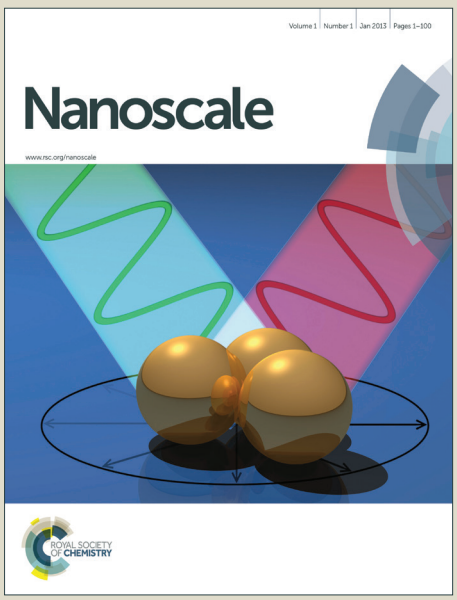





ROYAL SOCIETY OF CHEMISTRY

www.rsc.org/nanoscale

Cite this: DOI: 10.1039/c0xx00000x

www.rsc.org/xxxxxx

PAPER

# Highly branched platinum nanolance assemblies by polyallylamine functionalization as superior active, stable, and alcohol-tolerant oxygen reduction electrocatalysts †

**Gengtao Fu,[b] Xian Jiang,[b] Mingxing Gong,[b] Yu Chen,*[ab] Yawen Tang,[b] Jun Lin,[b] and Tianhong Lu[b]**

***Received (in XXX, XXX) Xth XXXXXXXXX 20XX, Accepted Xth XXXXXXXXX 20XX***
**DOI: 10.1039/b000000x**

The chemical functionalization of platinum (Pt) nanostructures becomes a new trend in electrocatalysts designs. Meanwhile, highly branched Pt nanostructures are highly exciting electrocatalysts with high activity and stability owing to their specific physical and chemical properties. In this work, the polyallylamine (PAH) functionalized Pt nanolance assemblies (Pt NLAs) have been successfully synthesized by chemical reduction of PAH–$Pt^{II}$ complex using formaldehyde (HCHO) in a two-phase water-complex system. The as-papered Pt NLAs are highly branched and three-dimensionally (3D) interconnected nanostructures, which are composed of many long Pt nanolances in various directions. The PAH functionalization improves the electrocatalytic activity of the Pt NLAs for the oxygen reduction reaction (ORR) because of high interface proton concentration on the Pt surface and excellent anti-oxidation ability of the Pt nanolances. Meanwhile, the PAH molecules bound on the Pt NLAs surface act as barrier networks to restrain accessibility of alcohol, exhibiting a high ORR selectivity. In addition, the PAH functionalized Pt NLAs show excellent durability for the ORR due to their particular 3D interconnected structure. The work demonstrates that the PAH functionalized Pt NLAs are indeed a promising cathodic electrocatalyst for the practical application of direct alcohol fuel cells.

## Introduction

Direct alcohol fuel cells (DAFCs), which directly convert chemical energy into electricity, have attracted considerable attention because of their fascinating features including low operating temperature, easy transportation and storage of the fuel, high energy density, and green emission.[1-5] However, there still remain several obstacles for the widespread commercialization of DAFCs. In particular, the poor performance of cathodic Pt electrocatalysts in the oxygen reduction reaction (ORR), including the sluggish ORR kinetics, performance degradation due to alcohol crossover, and weak long-term stability, has become one of the main bottlenecks in improving overall performance of DAFCs.[1-5]

Over the past decades, based on the manipulation of the geometric and electronic structures of Pt electrocatalysts, various effective strategies for improving the ORR activity have successfully developed, which mainly involve (i) controlling the morphology of Pt nanocrystals,[1] (ii) alloying Pt with other transition metals,[2] (iii) depositing Pt monolayers onto other metal nanoparticles to create core-shell structures,[3] and (iv) anchoring Pt nanoparticles on various supporting materials with specific function.[4] Although the conventional opinion is that the use of a capping agent in a wet-chemistry route undermines the overall catalytic activity of the metal nanoparticles because of the lack of ‘‘clean’’ surface active sites, at present, the chemical functionalization of metal surface becomes a new trend in designing electrocatalysts, which is based on the modification of the metal surface by nonmetallic molecules that can influence the hydrophilicity and electronic property of the metal or block the adsorption of poisoning species.[6-10] For example, Tong group reported that the adsorbed polyvinylpyrrolidone had the ability to significantly enhance the catalytic activity of the underlying Pt black towards both methanol and formic acid electrooxidations, and the degree of the enhancement was tunable by varying the polyvinylpyrrolidone content.[7] In particular and regarding the ORR in acidic media, Markovic group demonstrated that the ORR activity on the cyanide functionalized Pt{111} facets showed a 25-/10-fold increase in the $H_2SO_4$/$H_3PO_4$ electrolytes compared to the naked Pt{111} facets, where cyanide adsorbates on Pt surface indeed acted as a third body and consequently selectively blocked the adsorption of sulfuric and phosphoric acid anions.[8, 9]

Although Pt is the best ORR electrocatalyst, its electrocatalytic activity is not selective for the ORR. In DAFCs, the alcohol transport through perfluorosulphonate membranes to the cathode compartment (*i.e.*, so-called "alcohol crossover") generally occurs by diffusion as a result of the concentration gradient. Because Pt electrocatalysts are highly active for alcohol oxidation and the cathode potential is high, the alcohol oxidation reaction and the ORR take place at the same time. The mixed potential that results from the two simultaneously reactions not only severely reduces the cell voltage but also generates additional water and increases the required oxygen stoichiometric ratio.[11, 12] To overcome the

alcohol crossover effect, various transition-metal macrocycles and Pd-based alloy nanomaterials have been widely exploited as the Pt-alternative electrocatalysts for the ORR. However, these Pt-free electrocatalysts generally present less ORR activity and inferior long-term stability compared with the Pt-based electrocatalysts.[5] Therefore, this issue of alcohol crossover must be addressed from the perspective of the cathodic Pt electrocatalysts themselves in order to achieve a viable commercialization of DAFCs. Till now, considerable progress has been achieved in the synthesis of the alcohol-tolerant Pt-based electrocatalysts.[13, 14] Very recently, Markovic group demonstrated that calix[4]arene molecules functionalized Pt{111} facets or commercial Pt nanoparticles could efficiently suppress the ORR while fully preserve the Pt-like activity for the hydrogen oxidation reaction in $HClO_4$ electrolyte.[10] This unique selectivity was attributed to very strong ensemble effects in which the number of bare Pt sites available for adsorption of $O_2$ was much smaller than that for the adsorption of $H_2$ and the subsequent hydrogen oxidation reaction. These key findings demonstrate that the chemical functionalization of the Pt electrocatalysts may be regarded as a hopeful way to achieve the high ORR selectivity by selecting an appropriate modified molecule.

During fuel cells operation, the spheric Pt nanoparticles usually undergo aggregation, dissolution and Oswald ripening because of their high surface energy and zero-dimensionally (0D) structural feature, which induce enormous loss of the electrochemical surface area (ECSA) and thus decrease in the overall fuel cells performance.[15, 16] In recent years, the durability of cathodic Pt electrocatalysts has been recognized as an important issue for preserving fuel cells performance. Various effective strategies have been developed to improve the durability of the cathodic Pt electrocatalysts, including preparation of alloys consisting of Pt and other transition metals, replacement of carbon support with a conductive metal oxide, synthesis of core-shell Pt nanostructures, and one-dimensional (1D) Pt nanostructures, *etc*.[17-22] In particular, the three-dimensionally (3D) interconnected Pt nanoassemblies consisted of 1D Pt nanostructures show superior activity and durability for the ORR than 0D Pt nanoparticles, owing to high porosity, good flexibility, large surface area per unit volume, and interconnected open-pore structures.[15, 16] For instance, after an accelerated durability test, the self-supported interconnected Pt nanoassemblies lost only 16% of the initial Pt ECSA, while the commercial Pt black and Pt/C catalysts lost 85% and 95% of their initial ECSA.[15] At now, however, it is still a significant challenge to develop a direct synthesis method for the 3D Pt nanoassemblies with peculiar morphology.

Herein, we report for the first time a facile and one-pot hydrothermal methodology for the synthesis of polyallylamine (PAH, Scheme S1) functionalized Pt nanolance assemblies (Pt NLAs) by chemical reduction of PAH–$Pt^{II}$ complex using HCHO in a two-phase water-complex system. The PAH functionalized Pt NLAs with highly branched structure are composed of single-crystalline Pt nanolances as building blocks. Such Pt nanoassemblies meet the requirements of high ORR activity, excellent alcohol tolerance and superior durability.

## Experimental section

### Reagents and chemicals

Polyallylamine hydrochloride (PAH, weight-average molecular weight 15 0000) was supplied from Nitto Boseki Co., Ltd (Tokyo, Japan). Potassium tetrachloroplatinate(II) ($K_2PtCl_4$) and formaldehyde (HCHO) solution (40%) were purchased from Sinopharm Chemical Reagent Co., Ltd (Shanghai, China). High pure sulfuric acid ($H_2SO_4$) and perchloric acid ($HClO_4$) were purchased from Sigma-Aldrich (USA). Commercial Pt black was purchased from Johnson Matthey Corporation. Other reagents were of analytical reagent grade and used without further purification.

### Synthesis of the Pt nanolance assemblies (Pt NLAs)

In a typical synthesis, 2 mL of 0.025 M $K_2PtCl_4$ and 1.0 mL of 0.50 M PAH (molarity of PAH given with respect to the repeating unit) were added into 7.0 mL of water with continued stirring (molar ratio of PAH monomer to $Pt^{II}$ species was 10:1).[23] The interaction between $K_2PtCl_4$ and PAH resulted in the generation of the PAH-$Pt^{II}$ complex.[23] After adjusting solution pH to 0.5 using a 12 M HCl solution, the homogeneous solution was changed to a water-complex liquid-liquid two-phase system, as shown in **Scheme 1**. Subsequently, 0.5 mL of HCHO solution (40%) was added into the two-phase system. Then, the mixture solution was transferred to a 20-mL Teflon-lined stainless-steel autoclave, and was then heated at 140 ℃ for 6 h. After being cooled to room temperature, the obtained Pt NLAs were separated by centrifugation at 15000 rpm for 15 min, washed several times with water, and then dried at 60 ℃ for 5 h in a vacuum dryer.


**Scheme 1.** Digital photographs of PAH–$Pt^{II}$ complex solution before and after addition of HCl solution.

### Physical characterization

Scanning electron microscopy (SEM) images were taken on a JSM-2010 microscopy at an accelerating voltage of 20 kV. Energy dispersive X-ray (EDX) analysis of particles was carried out on a JEOL JSM-7600F SEM. Transmission electron microscopy (TEM) images were made on a JEOL JEM-2100F transmission electron microscopy operated at an accelerating voltage of 200 kV. The samples were prepared by placing a drop of the colloidal solution or catalyst powder dispersion in ethanol solution (99%) on a carbon film coated Cu grid (3mm, 300 mesh), followed by drying under ambient conditions. Fourier transform infrared (FT-IR) spectroscopy measurements were carried out on a Nicolet 520 SXFTIR spectrometer. X-ray diffraction (XRD) patterns were obtained with a Model D/max-rC X-ray diffractometer using Cu K$\alpha$ radiation source ($\lambda$= 1.5406 Å) and operating at 40 kV and 100 mA. High-resolution X-ray photoelectron spectroscopy (XPS) measurements were carried out on a Thermo VG Scientific ESCALAB 250 spectrometer with an Al K$\alpha$ radiator, and the vacuum in the analysis chamber was

maintained at about $10^{-9}$ mbar. The binding energy was calibrated by means of the C 1s peak energy of 284.6 eV. Thermogravimetric analysis (TGA) was performed on a Perkin Elmer thermogravimetric analyzer under $N_2$ atmospheres over a temperature range of 20–1000 °C with a ramp rate of 10 °C $min^{-1}$.

**Electrochemical measurements**

All electrochemical experiments were performed by using a CHI 660 C electrochemical analyzer (CH Instruments, Shanghai, Chenghua Co.). A standard three-electrode system was used for all electrochemical experiments, which consisted of a Pt wire as the auxiliary electrode, a saturated calomel reference electrode protected by Luggin capillary with KCl solution as the reference electrode, and a catalyst modified glassy carbon electrode as the working electrode. Rotating disk electrode test was performed on Gamry's Rotating Disk Electrode (RDE710) with a glassy carbon disk. Potentials in this study were reported with respect to the reversible hydrogen electrode (RHE). All electrochemical measurements were carried out at 30 ±1 °C.

Prior to electrochemical tests, the Pt NLAs were treated with UV/Ozone (wavelength at 185 and 254 nm in air for 4 h) to remove the most capping agent (*i.e.*, PAH).[23] For preparation of working electrode, a previously reported procedure was used.[24] In brief, a stock solution of 20% isopropanol and 0.02% Nafion® solution was prepared by mixing 20 mL of isopropanol with 79.6 mL of pure water and 0.4 mL of 5 wt% Nafion® solution ($V_{water}$: $V_{isopropanol}$: $V_{5\%\ Nafion}$ = 0.8: 0.2: 0.005) in a 100 mL volumetric flask. Next, 10 mg of the catalyst was measured into a 10 mL borosilicate vial and 5 mL of the stock isopropanol/Nafion® solution was added; The catalyst ink was then transferred to an ultrasonicator and sonicated for ≥60 minutes in a water bath temperature <40 ℃. A 10 μL droplet of the well-dispersed ink was pipetted onto the glassy carbon electrode (5 mm diameter, 0.196 $cm^2$). After drying under a low flow of $N_2$ at 40 °C for 30 minutes in air, the working electrode was obtained, and the specific loading of metal on the electrode surface was about 51 μg $cm^{-2}$.

Cyclic voltammetry (CV) measurements were carried out in $N_2$-saturated 0.5 M $H_2SO_4$ or 0.1 M $HClO_4$ solutions at a sweep rate of 50 mV $s^{-1}$. The ECSA of Pt electrocatalysts was calculated from the equation (ECSA=Q/m × C) by measuring the charge collected in the hydrogen adsorption/desorption region after double-layer correction.[1] *Q* is the charge in the hydrogen adsorption/desorption area. *m* is the loading amount of Pt metal, and *C* is the charge required for monolayer adsorption of hydrogen on a Pt surface (*C*=0.21 mC $cm^{-2}$).

Upon completion of the CV measurements, the saturation gas is switched to $O_2$, and the 0.5 M $H_2SO_4$ or 0.1 M $HClO_4$ electrolytes is saturated for ⩾25 minutes with $O_2$. The ORR polarization curves were obtained by sweeping the potential from 1.1 to 0.10 V (vs. RHE) at the scan rate of 5 mV $s^{-1}$ and rotation rate of 1600 rpm. Based on the ORR polarization curves, the kinetic current density ($i_k$) was calculated using the Koutecky-Levich equation ($1/i=1/i_k+1/i_l$),[23] Where $i_l$ and *i* were the limited diffusion current density and the measured current density, respectively.

The accelerated durability tests (ADT) were conducted by continuously cycling the potential between 0.6 and 1.2 V (vs. RHE) in $O_2$-saturated 0.5 M $H_2SO_4$ solution at a scan rate of 100 mV $s^{-1}$. Meanwhile, full-scale voltammogram between 0.0 and 1.2 V (vs. RHE) in $N_2$-saturated 0.5 M $H_2SO_4$ solution were recorded periodically to track the degradation of Pt electrocatalysts. The electrocatalytic oxidation of alcohol at electrocatalysts was done in an $N_2$-saturated 0.5 M $H_2SO_4$ solution with 1.0 M alcohol at a scan rate of 50 mV $s^{-1}$. The study of methanol tolerant ability for the ORR was done in an $O_2$-saturated 0.5 M $H_2SO_4$ solutions with 1.0 M methanol using RDE710 at a rotation rate of 1600 rpm and a sweep rate of 5 mV $s^{-1}$.

## Results and discussion

**Physicochemical characterization of the Pt NLAs**

The morphologies of the as-prepared Pt nanocrystals were firstly investigated by SEM. As observed, the Pt nanocrystals are 3D interconnected assemblies composed of a dozen or more main branches (Fig. 1A). The magnified SEM image reveals that every branch is constructed with the stem and the head, which looks like lance structure (Fig. 1B). The diameter of the nanolance is about 5~15 nm and the length is about 50~200 nm. A further insight into the morphology of the Pt nanocrystals was obtained from TEM image (Fig. 1C), confirming the interconnected lance-like structure. Surprisingly and interestingly, these nanolances are interconnected at a center, indicating that the formation of the Pt NLAs may involve growth from a common point rather than the simple aggregation of preformed nanoparticles.[15] Additionally, many of nanolances have smaller sub-branches growing from the main trunk with different angles, implying that the Pt nanolances grow along different directions. An individual Pt NLAs is shown in Fig. 1D. The selected-area electron diffraction (SAED) pattern of the individual Pt NLAs displays discontinuous concentric rings, composed of bright discrete diffraction spots (insert in Fig. 1D), indicating the high crystallinity degree of the Pt NLAs. The high-resolution TEM (HRTEM) image shows a connection region between one of the stem and the corresponding head (Fig. 1E). The corresponding SAED pattern reveals that the connectional region between stem and head is single-crystalline structure (insert in Fig. 1E). The magnified HRTEM images taken from regions a, b, c, and d marked by squares in Fig. 1E were displayed in Fig. 1F. The continuous fringes run through whole stem and head, suggesting that the connection between stem and head is not simply a physical contact but rather like an epitaxial growth.[25] The intervals between the two lattice fringes is found to be ca. 0.198 nm, close to the {100} lattice spacing of face centered cubic (*fcc*) Pt crystal (JCPDS no. 04-0802, 0.196 nm). TEM analyses indicate that the successive generations from stem to head of the nanolance grow along the <100> direction (*i.e.*, both belong to the same crystal system with nearly the same crystal orientation). Similar to the case of amine-assisted synthesis of the Pt nanocrystals with high-index facets,[26] the appearance of abundant Pt {100} facets at the Pt NLAs mainly arises from the prefer adsorption of amine groups on the high energy Pt {100} facets.[23, 27] In addition, clear lattice fringes indicate that the Pt NLAs maintain few low-coordination defect atoms. The previous investigations have demonstrated that smooth, defect-free, and crystalline Pt surface improved the ORR

activity of Pt electrocatalysts.[28] Thus, the highly crystalline Pt NLAs are believed to be a good candidate for the cathodic electrocatalysts due to the less lattice imperfection (*i.e.*, the less dislocations and stacking faults).

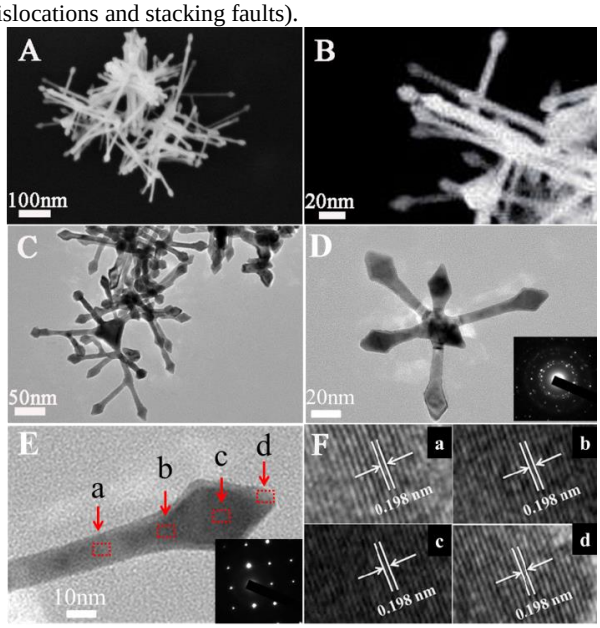


**Fig. 1** (A) Typical SEM and (B) magnified SEM images of the Pt NLAs. (C) Typical TEM and (D) magnified TEM images of the Pt NLAs. The bottom-right inset in (D) is corresponding SAED pattern. (E) HRTEM image of the Pt NLAs. The bottom-right inset in (E) is corresponding SAED pattern. (F) Magnified HRTEM images taken from regions a, b, c, and d marked by squares in (E), respectively.

PAH–$Pt^{II}$ complex is an organic coordination polymers. $Pt^{II}$ species highly concentrate on the carbon chain backbone of liquid-phase complex rather than disperse uniformly in water under the present experimental conditions (Scheme 2), which restrains the Brownian motion of the $Pt^{II}$ species. Upon reduction, the individual Pt nucleation connects with each other one-by-one along the scaffold direction of the carbon chain owing to strong Pt-N bond interaction between Pt nucleation and PAH, thus resulting in the formation of 1D Pt nanolances. Meanwhile, Pt crystal nuclei randomly grow along carbon chain backbone of complex in various directions owing to high concentration of $Pt^{II}$ species in liquid-phase complex, thus resulting in the formation of highly branched Pt nanostructures. The above-mentioned mode of formation may explain the growth mechanism of the Pt NLAs. However, the detailed mechanism needs further investigation.

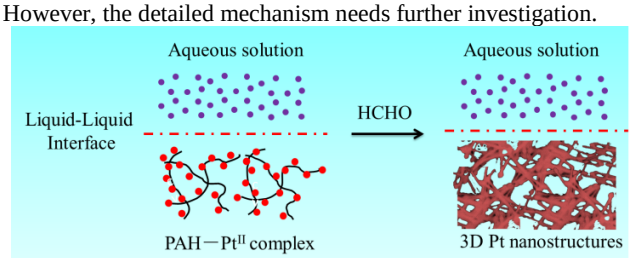


**Scheme 2** The mechanism formation of 3D interconnected Pt nanostructures in the water-complex liquid-liquid two-phase system.

The crystal structure and chemical composition of the as-synthesized Pt NLAs were characterized by EDX and XRD. EDX analysis demonstrates that the Pt NLAs mainly contain Pt element (Fig. 2A). XRD pattern shows the Pt NLAs have four peaks corresponding to the (111), (200), (220) and (311) facets of *fcc* Pt (JCPDS no. 04-0802), respectively (Fig. 2B). Meanwhile, the intensity ratio of (111) peak to (200) peak for the Pt NLAs is about 1.80, which is smaller than that of the standard value calculated from Pt JCPDS data (2.16). The result confirms that the Pt NLAs have a (100) dominated crystalline structure, in consistent with the HRTEM characterization.

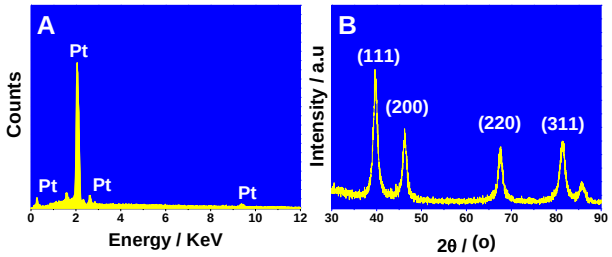


**Fig. 2** (A) EDX spectrum and (B) XRD pattern of the Pt NLAs.

The electronic structure and element state of Pt atoms in the Pt NLAs were qualitatively characterized by XPS. The most intense doublet of peaks, measured at 71.3 (Pt 4f7/2) and 74.5 eV (Pt 4f5/2), are ascribed to the $Pt^0$, while the weaker one with peaks at 72.3 (Pt 4f7/2) and 76.5 eV (Pt 4f5/2) are assigned to $Pt^{II}$ (Fig. 3A). By measuring the relative peak areas, the percentage of $Pt^0$ species in the Pt NLAs is calculated to be 93.1%. The Pt NLAs possess a lower amount of oxide state ($Pt^{II}$, 6.9%) compared with the commercial Pt black ($Pt^{II}$, 20.8%), indicating that the Pt NLAs have a weaker oxophilicity (Fig. 3A). On the other hand, the Pt NLAs have a ~0.5 eV decrease in electron binding energy compared with the commercial Pt black. FT-IR spectrum of the Pt NLAs is similar to that of pure PAH (Fig. S1, EIS†), showing the Pt NLAs are covered with PAH molecules. The binding of PAH on Pt NLAs surface was visualized by EDX mapping (Fig. 3B). The N element mapping pattern is identical with Pt element mapping pattern, indicating the uniform distribution of PAH on the Pt NLAs surface. Due to the strong N-Pt interaction between PAH and noble metal atom,[23, 29] the binding of PAH on Pt NLAs surface is responsible for the shift of Pt binding energy. Specifically, N atom in PAH has a high electron density due to the lone pair electrons of $–NH_2$ groups, and hence Pt atoms withdraw electrons from the neighboring N atoms in PAH. This, consequently, results in excellent anti-oxidation ability of the Pt NLAs due to the weaken $O_2$ adsorption originated from the decrease in 5d vacancies in Pt.[30] Obviously, the high percentage amount of $Pt^0$ species in the Pt NLAs is benefit for improving ORR activity because the oxide species on Pt surface is inactive for the ORR.

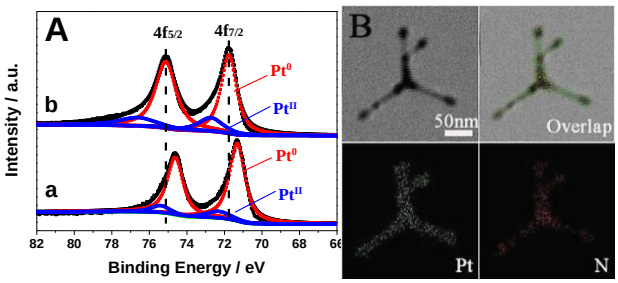


**Fig. 3** (A) XPS spectra of (a) the Pt NLAs and (b) commercial Pt black in the Pt 4f region. (B) EDX mapping of the Pt NLAs.

### Electrocatalytic performance for the ORR

The Pt NLAs were tested for possible use as a cathodic ORR electrocatalyst in DAFCs. The electrocatalytic activity of Pt NLAs was compared with commercial Pt black (Johnson Matthey) using the same Pt loading. The ORR activity of Pt electrocatalysts is generally dependent on the reaction medium. In $H_2SO_4$, Pt {100} facets are more active for the ORR than in nonadsorbing $HClO_4$ due to the bisulfate anion adsorption.[31] It has been established that the peak at 0.05–0.15 V corresponds largely to hydrogen adsorption at surface defects or corners/edges or (110) facets whereas the peak at 0.20–0.30 V corresponds largely to hydrogen adsorption at (100) faces.[32, 33] As observed, the Pt NLAs display a higher (100) peak while the Pt black show a higher (111) peak (Fig. 4A), also confirming that the Pt NLAs mainly consist of Pt{100} facets. The ECSA of the Pt NLAs (11.2 $m^2$ $g^{-1}$) is smaller that of the commercial Pt black (17.5 $m^2$ $g^{-1}$) based on the CV data. The lower ECSA for the Pt NLAs is most likely due to the large size of the Pt NLAs (diameter: 5~15 nm; length: 50~200 nm) compared with that of commercial Pt black (8.5 nm).[15]

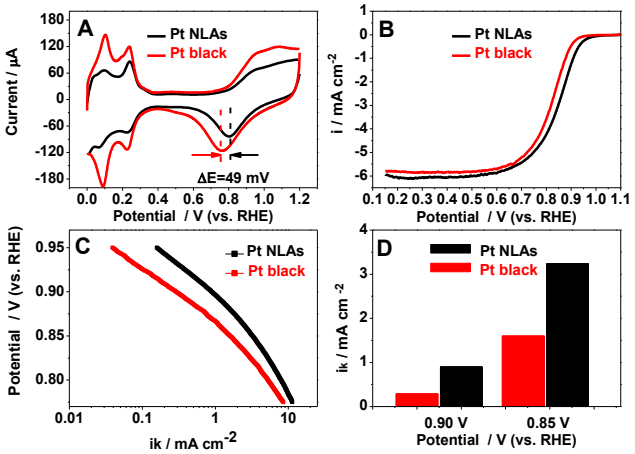


**Fig. 4** (A) CVs for the Pt NLAs and commercial Pt black in $N_2$-saturated 0.5 M $H_2SO_4$ solution at 50 mV $s^{-1}$. (B) ORR polarization curves for the Pt NLAs and commercial Pt black in $O_2$-saturated 0.5 M $H_2SO_4$ solution at a scan rate of 5 mV $s^{-1}$ and rotation rate of 1600 rpm. (C) The $i_k$ for the Pt NLAs and commercial Pt black at different potentials. (D) The $i_k$ values of the Pt NLAs and commercial Pt black at a fixed potential of 0.85 and 0.9 V for the ORR.

It is worth noting that the onset potential for surface oxide formation ($Pt + H_2O \rightarrow Pt–OH + H^+ + e^-$) and the following oxide reduction peak potential on the Pt NLAs show obvious positive shift compared to the commercial Pt black, suggesting fast hydroxyl adsorption/desorption on the Pt NLAs surface at more positive potentials. It is clear that the hydroxyl species preferentially adsorb on defect atoms.[28] Thus, the change of electronic structure of Pt atoms originated from PAH functionalization (*i.e.*, excellent anti-oxidation ability of the Pt NLAs) and single crystal structure of the Pt NLAs (*i.e.*, the few low-coordination defect atoms) contribute to delaying surface oxidation toward higher potentials. Moreover, it is observed that the Pt NLAs without UV-Ozone treatment show very small Pt oxidation peak compared to the treated Pt NLAs in CV measurements (Fig. S2). Thus, the positive shift of the reduction peak of Pt oxide on the Pt NLAs is also likely caused by the decreases of the Pt active sites due to adsorbed PAH on the Pt NLAs surface. Since adsorbed hydroxyl species inhibit the Pt ORR activity, the delay in the Pt−OH formation is benefit for improving Pt ORR activity. The typical ORR polarization curves of the Pt NLAs and Pt black in $O_2$-saturated 0.5 M $H_2SO_4$ solution at 1600 rpm are displayed in Fig. 4B. The current density is normalized in reference to the geometrical area of the glassy carbon electrode. A well-defined plateau on the potential starting from 0.10 to 0.60 V (vs. RHE) and a steep feature between 0.60 to 0.95 V (vs. RHE) are known as the diffusion-controlled and mixed kinetic-diffusion control region, respectively. The ORR activity can be visually benchmarked from its half-wave potential ($E_{1/2}$, the point half-way between zero current and the diffusion limited current density plateau). According to the definition, $E_{1/2}$ of the Pt NLAs is about 0.85 V, which shows a 30 mV shift to more positive potentials compared to commercial Pt black (0.82 V), indicating dramatically improved ORR kinetics for the Pt NLAs. Although ECSA of the Pt NLAs is much lower than that of commercial Pt black, the Pt NLAs have a bigger diffusion-limiting current density for the ORR than commercial Pt black at 0.1 V. As shown by SEM image, the Pt NLAs have the particular 3D network-like architecture, which can improve mass transport of $O_2$ to the Pt sites and consequently increase the diffusion-limiting current density for the ORR.[1, 15]

The area-specific current density ($i_k$), which represents the intrinsic activity of the electrocatalysts and is calculated from Koutecky-Levich equation, is a better indicator of an electrocatalysts' quality. The tafel plots for $i_k$ at the Pt NLAs and commercial Pt black are displayed in Fig. 4C. As observed, the Pt NLAs show greatly improved specific kinetic activity compared to the Pt black in the whole potential range. For instance, as illustrated in Fig. 4D, $i_k$ of the Pt NLAs at 0.85 V (3.24 mA $cm^{-2}$) and 0.9 V (0.90 mA $cm^{-2}$) is 2.03 and 3.10 times greater than that of Pt black at 0.85 V (1.60 mA $cm^{-2}$) and 0.9 V (0.29 mA $cm^{-2}$), respectively. In addition, the $i_k$ of the Pt NLAs at 0.90 V (0.90 mA $cm^{-2}$) is also much higher than those of Pt-on-Pd bimetallic nanostructures (0.67 mA $cm^{-2}$),[34] Pt-hollow nanostructures (0.529 mA $cm^{-2}$),[35] and nanoporous-$Pt_1Ni_1$ alloys (0.307 mA $cm^{-2}$),[36] indicating that the Pt NLAs show more competitive electrocatalytic activity for the ORR.

The ORR activities of electrocatalysts were also investigated in 0.1 M $HClO_4$ solution. The CV datas show that the potentials for surface-oxide formation and the following reduction on the Pt NLAs also positively shift by ca. 21 mV compared to the commercial Pt black (Fig. 5A). ORR measurements demonstrate the *E*1/2 of the Pt NLAs shows a 20 mV positive shift compared to commercial Pt black (Fig. 5B). These electrochemical results clearly indicate that the Pt NLAs with Pt {100} facets also show an improved ORR activity in $HClO_4$ solution. Obviously, only facets effect is not sufficient to explain the enhanced ORR activity of the Pt NLAs in both $H_2SO_4$ and $HClO_4$ solution.

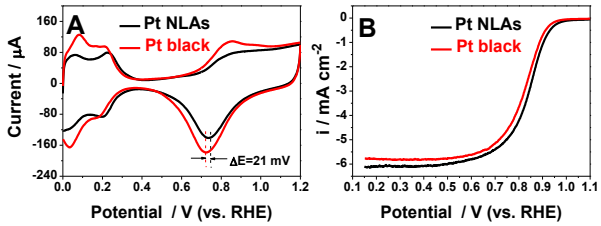


**Fig. 5** (A) CVs for the Pt NLAs and commercial Pt black in $N_2$-saturated 0.1 M $HClO_4$ solutions at 50 mV $s^{-1}$. (B) ORR polarization curves for the Pt NLAs and commercial Pt black in $O_2$-saturated 0.1 M $HClO_4$ solution at a scan rate of 5 mV $s^{-1}$ and rotation rate of 1600 rpm.

It is well known that the ORR consists of four proton transfers and four electron transfers to each $O_2$ molecule (*i.e.*, $O_2 + 4H^+ + 4e^- \rightarrow 2H_2O$).[37, 38] On the Pt atom surface, the ORR overpotential strongly relates to the hydrogenation of oxygen (*i.e.*, $O_2 + H^+ + e^- \rightarrow OOH^*$) or protonation process of the adsorbed intermediates such as O* and OH* (*i.e.*, $O^* + H^+ + e^- \rightarrow OH^*$; $OH^* + H^+ + e^- \rightarrow H_2O^*$; where * denotes an adsorbed species).[37] The very recent DFT calculations even indicated the rate-determining step of the ORR on the Pt atom surface was the protonation process of O* or OH* species.[38] Thus, the ORR activity relates to the surrounding $H^+$ concentration at the Pt surface. In present case, PAH not only anchor to the Pt NLAs surfaces but also increase the local $H^+$ concentrations on Pt atoms at the Pt NLAs/electrolyte interface compared to bulk $H^+$ concentration of 0.1 M $HClO_4$ solution. Our previous works have indicated that PAH have excellent chemical stability. The PAH molecules adsorbed on Pt surface can not be completely removed by UV/ozone treatment.[23] After UV/ozone treatment, the TGA curve of the pre-treated Pt NLAs show a weight loss of 12.83% in the temperature range of 100 to 1000 °C (Fig. S3, EIS†), originating from a possible scission of the amine side-chains and the polymer backbone. Assuming that all $–NH_2$ groups in the adsorbed PAH molecules are completely protonated (*i.e.*, $–NH_3^+$), the $H^+$ amount on the Pt NLAs is calculated to be $1.57\times10^{-3}$ mol $_{H+}$ $g^{-1}_{Pt}$. Combining with ECSA of the Pt NLAs, the proton coverage on the Pt NLAs surface is $1.4\times10^{-8}$ $mol^1_{H+}$ $cm^{-2}_{Pt}$, which is much bigger than the hypothetical interface proton concentration in bulk 0.1 M $HClO_4$ solution ($1.87\times10^{-11}$ $mol^1_{H+}$ $cm^{-2}$), as shown in Scheme 3. Thus, the high interface $H^+$ concentration at the Pt NLAs surface improves the Pt ORR activity.

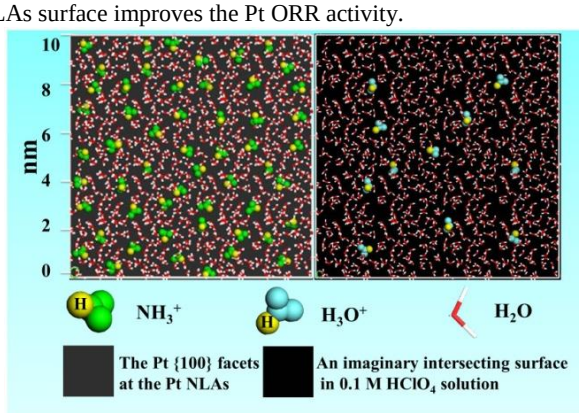


**Scheme 3** The proton coverage on the Pt NLAs surface (Left). The interface proton concentration of 0.1 M $HClO_4$ solution at an imaginary intersecting surface (Right).

One of the major problems in DAFCs is the alcohol crossover that deteriorates cathodic Pt electrocatalysts and the need for alcohol tolerance in the cathodic electrocatalysts to ensure a good cell performance.[39] In this study, the alcohol tolerance of the Pt NLAs was investigated by using methanol as a representative alcohol molecule. Fig. 6A shows the typical ORR polarization curves of the Pt NLAs and Pt black in $O_2$-saturated 0.5 M $H_2SO_4$ solution at 1600 rpm in the absence and presence of 1.0 M methanol. The ORR polarization curve of commercial Pt black displays that current density reversal culminating in "valleys" (maximum current densities, 900 μA $cm^{-2}$) formed around 0.80 V (vs. RHE) and the overpotential increased by ca. 400 mV in the presence of methanol. The observed behaviour is caused by the competition between methanol oxidization reaction and ORR on the Pt surface, resulting in the negation of the ORR current by the methanol oxidation current. In contrary, the ORR activity of the Pt NLAs is much less affected by methanol, indicating that Pt NLAs exhibits a high ORR selectivity in the presence of methanol (Fig. 6B). Furthermore, the alcohol tolerance of electrocatalysts was further investigated by performing CV in $N_2$-saturated 0.5 M $H_2SO_4$ with 1.0 M methanol solution (Fig. S4, EIS†). The CV data reveals an obvious methanol oxidation peak at 0.88 V for commercial Pt black in positive scan direction. However, the oxidation current is not obvious for the Pt NLAs, indicating strong electrochemical resistance against methanol oxidation at the Pt NLAs.

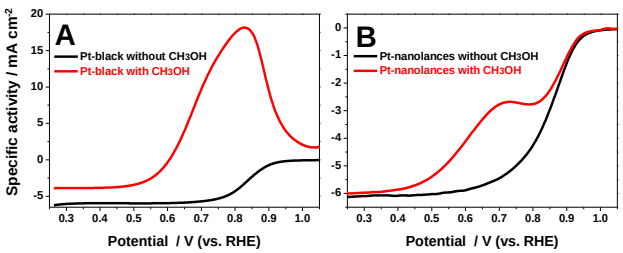


**Fig. 6** Comparison of ORR polarization curves of (A) the commercial Pt black and (B) Pt NLAs in $O_2$-saturated 0.5 M $H_2SO_4$ with and without the presence of 1.0 M methanol at a scan rate of 5 mV $s^{-1}$ and rotation rate of 1600 rpm.

As shown in mentioned EDX mapping in Fig. 3B, PAH molecules uniformly bind to the Pt NLAs surface, which can act as barrier networks to restrain accessibility of methanol on Pt surface due to its lager molecule size (size: 2.1 Å) than oxygen molecule (size: 1.2 Å) (Scheme 4). In order to further confirm the mechanism, the electrooxidation of ethanol (size: 3.3 Å) and 1-propanol (size: 4.8 Å) on the Pt NLAs and black were also investigated by CV. It is observed that ECSA specific activity of the Pt NLAs decrease with increasing molecule size of alcohol molecules, relative to the Pt black (Fig. S5, EIS†). After removing PAH layer on the Pt NLAs surface by acetic acid washing,[40] the acetic acid-cleaned Pt NLAs show superior electrocatalytic activity for the methanol electrooxidation compared to initial PAH functionalized Pt NLAs (Fig. S6, EIS†). To some extent, this fact confirms the block function of PAH barrier networks for the methanol accessibility. Of course, the possibility that PAH molecules block the active sites for methanol adsorption cannot be ruled out completely, and need further investigation in the future.

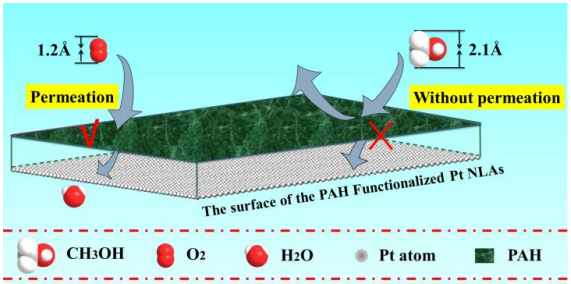


**Scheme 4** Schematic representation of the influence of the PAH barrier networks at the Pt NLAs surface on the accessibility of methanol molecule with big molecule size.

Besides the activity and selectivity, the durability is also a key issue for the commercialization of DAFCs. To evaluate the stability of the Pt NLAs, the accelerated durability tests (ADT) of electrocatalysts were conducted by continuously cycling the potential between 0.6 and 1.2 V (vs. RHE) in $O_2$-saturated 0.5 M $H_2SO_4$ solution, based on an established procedure.[1, 15] As observed, the current of the peaks in the hydrogen adsorption/desorption potential region (0.0–0.35V) for the commercial Pt black electrocatalyst dropped dramatically with increase of the number of CV cycles (Fig. 7A). In sharp contrast, the Pt NLAs exhibit only a slight drop for the current of the peaks under the same potential condition (Fig. 7B). Upon integration of the charge between 0 and 0.35 V (vs. RHE) associated with hydrogen adsorption, no recordable loss of surface area on Pt NLAs was observed (only ~6.8%), while ~46.3% loss of surface area on Pt black was observed (Fig. 7C). Furthermore, ORR polarization curves were also measured at 5000 cycle intervals. After 10000 cycles, there is only a 12 mV degradation in the half-wave potential $E_{1/2}$ for the Pt NLAs (Fig. 7D), while the corresponding potential $E_{1/2}$ for commercial Pt black decreases by 57 mV (Fig. S7, EIS†). The ADT results demonstrate that the Pt NLAs have remarkably higher stability compared to commercial Pt black. The particular interconnected structure that suppresses Ostwald ripening effect[1, 15] as well as abundant low energy Pt{100} facets and less defective single crystal nature that restrain electrochemical corrosion/dissolution of Pt nanoparticles at high potential[41] are responsible for the enhanced durability of the Pt NLAs. In addition, the electrochemical dissolution of Pt nanoparticles is also significantly affected by their particle size. The large size of the Pt NLAs (diameter: 5~15 nm; length: 50~200 nm) compared with that of commercial Pt black (8.5 nm) also contribute to the durability enhancement.

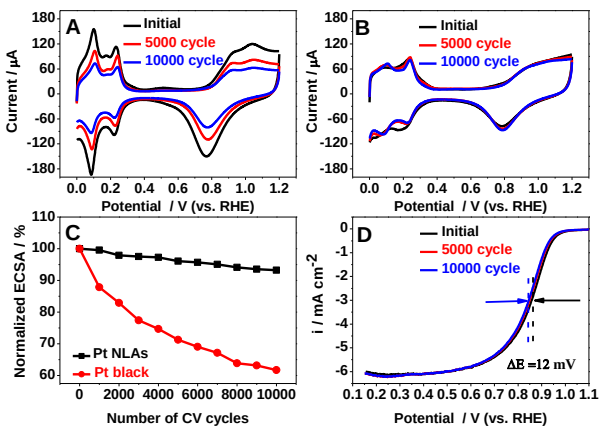


**Fig. 7** CVs for (A) the Pt NLAs and (B) commercial Pt black after prolonged cycles of CV tests. (C) Loss of ECSA of the Pt NLAs and commercial Pt black electrocatalysts with the number of CV cycles. (D) ORR polarization curves of the Pt NLAs after different numbers of cycles.

## Conclusions

In summary, PAH functionalized 3D Pt nanoassemblies consisting of 1D single crystal Pt nanolance are prepared by a facile hydrothermal reduction route in a two-phase water-complex system. Compared with the commercial Pt black, the as-synthesized Pt NLAs display an impressive eletrocatalytic performance for the ORR, such as high onset potential, excellent durability, and superior alcohol tolerance. The PAH functionalization not only improves the Pt ORR activity but also endows the Pt NLAs with particular selectivity for the ORR. The particular interconnected structure of nanoassembles and single crystal nature of Pt nanolance are responsible for excellent durability of the Pt NLAs for the ORR. We expect that this work will provide a promising strategy for developing efficient ORR electrocatalysts and can also be extended to the preparation of other metal nanostructures with desirable functions.

## Acknowledgements

This work was supported by NSFC (21376122, 21273116 and 21376122), Natural Science Foundation of Jiangsu Province (BK20131395), the United Fund of NSFC and Yunnan Province (U1137602), Industry-Academia Cooperation Innovation Fund Project of Jiangsu Province (BY2012001), Fundamental Research Funds for the Central Universities (GK201402016), and the Starting Funds of Shaanxi Normal University.

## Notes and references

[a] School of Materials Science and Engineering, Shaanxi Normal University, Xi'an 710062, PR China
E–mail: ndchenyu@gmail.com (Y. Chen)
[b] Jiangsu Key Laboratory of New Power Batteries, School of Chemistry and Materials Science, Nanjing Normal University, Nanjing 210023, PR China

†Electronic Supplementary Information (ESI) available: Experimental and characterization data. See DOI: 10.1039/b000000x/

1. S. H. Sun, G. X. Zhang, D. S. Geng, Y. G. Chen, R. Y. Li, M. Cai and X. L. Sun, *Angew. Chem. Int. Edit.*, 2011, **50**, 422-426.
2. S. J. Hwang, S. K. Kim, J. G. Lee, S. C. Lee, J. H. Jang, P. Kim, T.-H. Lim, Y. E. Sung and S. J. Yoo, *J. Am. Chem. Soc.*, 2012, **134**, 19508-19511.
3. B. Lim, M. J. Jiang, P. H. C. Camargo, E. C. Cho, J. Tao, X. M. Lu, Y. M. Zhu and Y. N. Xia, *Science*, 2009, **324**, 1302-1305.
4. Z. Wu, Y. Lv, Y. Xia, P. A. Webley and D. Zhao, *J. Am. Chem. Soc.*, 2011, **134**, 2236-2245.
5. Y. M. Tan, C. F. Xu, G. X. Chen, N. F. Zheng and Q. J. Xie, *Energy Environ. Sci.*, 2012, **5**, 6923-6927.
6. Y. J. Tong, *Chem. Soc. Rev.*, 2012, **41**, 8195-8209.
7. C. Susut, D.-J. Chen, S.-G. Sun and Y. J. Tong, *Phys. Chem. Chem. Phys.*, 2011, **13**, 7467-7474.

8. M. Escudero-Escribano, M. E. Zoloff Michoff, E. P. M. Leiva, N. M. Markovic, C. Gutierrez and A. Cuesta, *Chemphyschem*, 2011, **12**, 2230-2234.
9. D. Strmcnik, M. Escudero-Escribano, K. Kodama, V. R. Stamenkovic, A. Cuesta and N. M. Markovic, *Nat. Chem.*, 2010, **2**, 880-885.
10. B. Genorio, R. Subbaraman, D. Strmcnik, D. Tripkovic, V. R. Stamenkovic and N. M. Markovic, *Angew. Chem. Int. Edit.*, 2011, **50**, 5468-5472.
11. J. H. Yang, W. J. Zhou, C. H. Cheng, J. Y. Lee and Z. L. Liu, *ACS Appl. Mater. Interfaces*, 2010, **2**, 119-126.
12. C. X. Xu, Y. Zhang, L. Q. Wang, L. Q. Xu, X. F. Bian, H. Y. Ma and Y. Ding, *Chem. Mater.*, 2009, **21**, 3110-3116.
13. M. R. Gao, Q. Gao, J. Jiang, C. H. Cui, W. T. Yao and S. H. Yu, *Angew. Chem. Int. Edit.*, 2011, **123**, 5007-5010.
14. Z. H. Wen, J. Liu and J. H. Li, *Adv. Mater.*, 2008, **20**, 743-747.
15. B. Y. Xia, W. T. Ng, H. Bin Wu, X. Wang and X. W. Lou, *Angew. Chem. Int. Edit.*, 2012, **51**, 7213-7216.
16. S. Akbar, J. M. Elliott, M. Rittman and A. M. Squires, *Adv. Mater.*, 2013, **25**, 1160-1164.
17. V. R. Stamenkovic, B. Fowler, B. S. Mun, G. F. Wang, P. N. Ross, C. A. Lucas and N. M. Markovic, *Science*, 2007, **315**, 493-497.
18. J. Greeley, I. Stephens, A. Bondarenko, T. P. Johansson, H. A. Hansen, T. Jaramillo, J. Rossmeisl, I. Chorkendorff and J. K. NOrskov, *Nat. Chem.*, 2009, **1**, 552-556.
19. S. Q. Ci, J. P. Zou, G. S. Zeng, S. L. Luo and Z. H. Wen, *J. Mater. Chem.*, 2012, **22**, 16732-16737.
20. S.-Y. Huang, P. Ganesan, S. Park and B. N. Popov, *J Am Chem Soc*, 2009, **131**, 13898-13899.
21. J. X. Wang, C. Ma, Y. Choi, D. Su, Y. Zhu, P. Liu, R. Si, M. B. Vukmirovic, Y. Zhang and R. R. Adzic, *J. Am. Chem. Soc.*, 2011, **133**, 13551-13557.
22. H. Yang, *Angew. Chem. Int. Edit.*, 2011, **50**, 2674-2676.
23. G. Fu, K. Wu, X. Jiang, L. Tao, Y. Chen, J. Lin, Y. Zhou, S. Wei, Y. Tang, T. Lu and X. Xia, *Phys Chem Chem Phys*, 2013, **15**, 3793-3802.
24. Y. Garsany, O. A. Baturina, K. E. Swider-Lyons and S. S. Kocha, *Anal. Chem.*, 2010, **82**, 6321-6328.
25. X. Wen, Y. T. Xie, W. C. Mak, K. Y. Cheung, X. Y. Li, R. Renneberg and S. Yang, *Langmuir*, 2006, **22**, 4836-4842.
26. X. Huang, Z. Zhao, J. Fan, Y. Tan and N. Zheng, *J. Am. Chem. Soc.*, 2011, **133**, 4718-4721.
27. M. Chen, J. Kim, J. Liu, H. Fan and S. Sun, *J. Am. Chem. Soc.*, 2006, **128**, 7132-7133.
28. C. Koenigsmann, W.-p. Zhou, R. R. Adzic, E. Sutter and S. S. Wong, *Nano Lett.*, 2010, **10**, 2806-2811.
29. G. Fu, W. Han, L. Yang, J. Lin, S. Wei, Y. Chen, Y. Zhou, Y. Tang, T. Lu and X. Xia, *J. Mater. Chem.*, 2012, **22**, 17604-17611.
30. G. Fu, K. Wu, J. Lin, Y. Tang, Y. Chen, Y. Zhou and T. Lu, *J. Phys. Chem. C*, 2013, **117**, 9826-9834.
31. S. Guo and S. Sun, *J. Am. Chem. Soc.*, 2012, **134**, 2492-2495.
32. R. Loukrakpam, P. Chang, J. Luo, B. Fang, D. Mott, I. T. Bae, H. R. Naslund, M. H. Engelhardd and C. J. Zhong, *Chem. Commun.*, 2010, **46**, 7184-7186.
33. Y. Kang, M. Li, Y. Cai, M. Cargnello, R. E. Diaz, T. R. Gordon, N. L. Wieder, R. R. Adzic, R. J. Gorte, E. A. Stach and C. B. Murray, *J. Am. Chem. Soc.*, 2013, **135**, 2741-2747.
34. Z. M. Peng and H. Yang, *J. Am. Chem. Soc.*, 2009, **131**, 7542-7543.
35. Z. Peng, J. Wu and H. Yang, *Chem. Mater.*, 2009, **22**, 1098-1106.
36. R. Y. Wang, C. X. Xu, X. X. Bi and Y. Ding, E*nergy Environ. Sci.*, 2012, **5**, 5281-5286.
37. I. E. L. Stephens, A. S. Bondarenko, F. J. Perez-Alonso, F. Calle-Vallejo, L. Bech, T. P. Johansson, A. K. Jepsen, R. Frydendal, B. P. Knudsen, J. Rossmeisl and I. Chorkendorff, *J. Am. Chem. Soc.*, 2011, **133**, 5485-5491.
38. Z. Duan and G. Wang, *J. Phys. Chem. C*, **117**, 6284-6292.
39. S. B. Yin, M. Cai, C. X. Wang and P. K. Shen, E*nergy Environ. Sci.*, 2011, **4**, 558-563.
40. V. Mazumder and S. Sun, *J. Am. Chem. Soc.*, 2009, **131**, 4588-4589.
41. C. Koenigsmann, A. C. Santulli, K. Gong, M. B. Vukmirovic, W.-p. Zhou, E. Sutter, S. S. Wong and R. R. Adzic, *J. Am. Chem. Soc.*, 2011, **133**, 9783-9795.